Asian Journal of Chemistry; Vol. 38, No. 3 (2026), 824-834
ASIAN JOURNAL OF CHEMISTRY
https://doi.org/10.14233/ajchem.2026.35069

Preparation and Electrochemical Performance of Fe_3O_4:Gd@$NaYF_4$ Core-Shell Nanoparticles for Supercapacitor Applications

J. RAGAVIDURGA*, and T. SUMATHI

Department of Physics, Annamalai University, Annamalainagar, Chidambram-608002, India

*Corresponding author: E-mail: ragavidurga97@gmail.com

Received: 20 October 2025 *Accepted*: 19 February 2026 *Published online*: 6 March 2026 AJC-22302

Fe_3O_4:Gd@$NaYF_4$ core-shell nanoparticles were successfully synthesized using a facile hydrothermal method. The structural analysis confirmed a cubic crystal structure for the prepared core-shell nanoparticles, with an average crystallite size of 52 nm. FESEM and HRTEM studies revealed that the Fe_3O_4:Gd@$NaYF_4$ product consists of spherical nanoparticles with a core-shell architecture, which was corroborated by EDS mapping showing the distribution of Gd, Na, Y and F elements within the samples. XPS analysis further confirmed the surface composition and determined the valence states of the constituent elements, consistent with the $NaYF_4$ shell. Optical studies revealed indirect bandgap values of 3.60 eV for Fe_3O_4:Gd and 3.25 eV for the Fe_3O_4:Gd@$NaYF_4$ core-shell nanoparticles, respectively. The Fe_3O_4:Gd@$NaYF_4$ electrode exhibited pronounced pseudocapacitive behaviour in CV studies, delivering a substantial specific capacitance of 612 F g^{-1} at a current density of 1 A g^{-1}. This synergistic combination of pseudocapacitance and high conductivity results in better electrochemical performance, highlighting the strong potential of material for high-performance energy storage devices.

Keywords: Core-shell nanoparticles, Gadolinium, Optical properties, Electrochemical properties.

INTRODUCTION

In response to the energy crisis and environmental concerns, research into sustainable energy storage systems like supercapacitors has intensified. Supercapacitors are promising due to their high power, fast kinetics and long cycle life, however, their broad application is limited by low energy density, a property fundamentally governed by electrode materials [1-4]. Supercapacitors are generally classified into two main categories based on their charge storage mechanism *viz*. electrochemical double-layer capacitors (EDLCs) and pseudocapacitors. Electrochemical double-layer capacitors (EDLCs) store charge through electrostatic accumulation at the electrode-electrolyte interface, whereas pseudocapacitors store charge *via* fast and reversible surface redox reactions. Pseudocapacitance can offer a much higher intrinsic capacitance per surface area than EDLCs, with classic electrode materials including transition metal oxides and conducting polymers [5,6].

Transition metal oxides such as Co_3O_4 [7], $NiCo_2O_4$ [8], Fe_3O_4 [9], SnO_2 [10], MnO_2 [11], *etc.* are compelling as pseudocapacitance electrode materials due to the multivalent states of their metallic ions and their crystal shapes, which facilitate rapid faradaic redox processes. Among metal oxides, magnetite (Fe_3O_4) is a notable option due to its environmental sustainability, natural abundance, cost-effectiveness and diverse oxidation states [12]. Fe_3O_4 high theoretical capacitance is undermined in practice by poor conductivity, particle agglomeration and cycling instability. While gadolinium (Gd) doping can enhance conductivity and modify structure, key challenges persist. These include precisely controlling Gd incorporation to avoid detrimental phases and designing robust, binder-free electrode architectures for optimal charge transport and durability. Addressing these limitations requires innovative synthetic strategies that combine precise doping control with advanced nanostructuring techniques [13].

As summarized in Table-1, mostly reported core-shell nanomaterials employ conventional shell materials that offer limited functional versatility. Insulating oxides hinder reaction kinetics, conductive carbon suffers from limited durability and ion transport; and the bare active material, although highly reactive, lacks structural stability. The proposed Fe_3O_4:Gd@$NaYF_4$ core-shell system overcomes these limitations by incorporating an active shell that not only protects the core but also regulates charge transfer and promotes synergistic interactions.

TABLE-1
COMPARISON TO EXISTING MATERIALS IN PREVIOUSLY PUBLISHED CORE-SHELL SYSTEM

Material system	Core function	Shell/matrix function	Key advantages	Major limitations	Ref.
Fe_3O_4@SiO_2	Catalytic activity, magnetism	Inert barrier, surface for functionalization	Excellent biocompatibility; prevents aggregation; easy surface modification.	SiO_2 is electrically insulating, severely hindering charge transfer	[14]
Fe_3O_4@C	Catalytic activity, magnetism	Conductive protective layer	Good electrical conductivity; enhances electron transfer; protects core from acidic corrosion.	Graphitic carbon can be electrochemically oxidized at high potentials; limited functionality beyond conductivity.	[15]
Gd doped Fe_3O_4 (bare)	Enhanced catalysis *via* Gd^{3+} doping, magnetism	N/A	Improved catalytic activity over pure Fe_3O_4; Gd^{3+} introduces lattice strain and active sites.	Prone to oxidation and aggregation; lacks protection, leading to rapid performance degradation.	[16]
Fe_3O_4@TiO_2/ZrO_2	Catalytic activity, magnetism	Metal oxide protective layer	Good chemical/thermal stability; some oxide shells (TiO_2) can be semiconductive.	Often too thick or insulating, creating a significant charge-transfer barrier; interfacial resistance can be high.	[17]
$NaYF_4$:Ln^{3+} (standalone)	N/A (host matrix)	Upconversion luminescence, ion conductor	Excellent host for lanthanide ions; facilitates ion transport; optically active.	Lacks inherent magnetic or strong catalytic centers; poor electrical conductivity.	[18]
Fe_3O_4:Gd@$NaYF_4$	Gd-enhanced capacitance & magnetism	Protective, ion-conductive, & functional interface	Synergistic combo: (1) Robust $NaYF_4$ shield prevents corrosion/aggregation; (2) Y^{3+} doped shell mediates ion transfer & reduces recombination; (3) Maintains core's magnetic & catalytic properties.	Synthesis can be more complex than single-shell systems; optimal shell thickness is critical for balancing protection *vs.* charge transfer.	Present work

This integrated architecture ensures enhanced stability, efficient charge mediation and preserved core functionality, resulting in improved and durable performance in sensing, catalytic and energy-related applications.

In this present work, core-shell nanostructures present a viable strategy to enhance the electrochemical performance of electrode materials. Among these, Fe_3O_4:Gd@$NaYF_4$ core-shell nanoparticles represent a novel multifunctional material with potential for supercapacitor applications. In this architecture, Gd doped Fe_3O_4 offers high theoretical capacitance and magnetic functionality, while the $NaYF_4$ shell can act as a protective and conductive matrix to improve cycling stability and electron transport. However, the application of this specific core-shell system in supercapacitors remains largely unexplored. The synthesis and electrochemical characterization of Fe_3O_4:Gd@$NaYF_4$ nanoparticles are therefore of significant interest, as advances in controlled fabrication could lead to improve the energy storage performance alongside possible multifunctional uses in bioimaging or optoelectronics [19,20].

EXPERIMENTAL

The solvents and chemicals *viz*. iron(II) sulphate heptahydrate ($FeSO_4·7H_2O$), gadolinium(III) nitrate ($Gd(NO_3)_3$), sodium sulphide flakes ($Na_2S·9H_2O$), ammonium iron(III) sulphate dodecahydrate ($NH_4Fe(SO_4)_2·12H_2O$), iron(III) sulphate ($Fe_2(SO_4)_3·5H_2O$), ammonium solution (NH_4OH), sodium sulphide (Na_2S), sodium fluoride (NaF), polyvinyl pyrrolidone (PVP) were purchased from Sigma Company and were high-purity grade. All chemicals were used without further purification.

Synthesis of Fe_3O_4:Gd nanoparticles: Fe_3O_4 nanoparticles were initially synthesized by dissolving $FeSO_4·7H_2O$ and $Fe_2(SO_4)_3·5H_2O$ (2 mmol each) in 100 mL of deionized water followed by the addition of 3.6 g Na_2S flakes and 1.0 g polymer to the reaction mixture under continuous stirring. Then, $Gd(NO_3)_3$ (5 mmol) solution was prepared in 50 mL of deionized water. These two homogeneous solutions were mixed together, the mixture was stirred energetically at 50 ºC for 30 min (pH ~12) and then transferred to a 100 mL Teflon-lined stainless-steel autoclave at 180 ºC for 6 h. After the completion of the reaction period, the autoclave was then allowed to cool to room temperature. The resulting black products was rinsed repeatedly with ethanol and then dried at 60 ºC for 6 h.

Synthesis of $NaYF_4$ nanoparticles: $NaYF_4$ nanoparticles were synthesized *via* a simple hydrothermal method, employing PVP as a surfactant to control their shape and crystal structure. First, aqueous solutions of 0.02 g PVP and 0.03 M $Y(CH_3COO)_3·4H_2O$ were prepared separately, each in 25 mL of deionized water. These solutions were then combined dropwise under stirring to form a uniform mixture. Next, 50 mL of 0.2 mol L^{-1} NaF solution was introduced dropwise into the mixture, followed by 1 h of stirring. The resulting suspension was centrifuged at 3000 rpm and washed sequentially with ethanol and deionized water. The collected precipitate was then subjected to hydrothermal treatment at 200 ºC for 24 h. After cooling to room temperature, the final product was centrifuged, separated and dried at 80 ºC for 6 h in an oven.

Synthesis of Fe_3O_4:Gd/$NaYF_4$ core-shell nanoparticles: Fe_3O_4:Gd@$NaYF_4$ core-shell nanocomposites were synthesized *via* a stepwise procedure. Initially, 2.82 g of upconversion nanoparticles (UCNPs) were dispersed in a mixed solvent of ethanol (60 mL) and deionized water (40 mL) less than 45 min of sonication. Subsequently, 0.02 g of PVP was introduced into the dispersion, followed by an additional hour of sonication. In parallel, 1.15 g of dried Fe_3O_4:Gd NPs were sonicated in 100 mL of water, with 3 mL of NH_4OH solution added dropwise over 1 h. The UCNP dispersion was then slowly introduced into the Fe_3O_4:Gd nanoparticles solution under vigorous stirring. After continuous stirring at room temperature for 2 h, the Fe_3O_4:Gd@$NaYF_4$ nanoparticles were magnetically separated and repeatedly washed with deionized water to eliminate non-magnetic impurities. The purified product was dried at 80 ºC for 10 h to remove residual solvents and subsequently annealed at 700 ºC for 2 h under controlled conditions to obtain the final core-shell nanoparticles.

Characterization: Thermal analysis was analyzed utilizing the NETZSCH-STA 449 F3 Jupiter instrument. Powder X-ray diffraction (XRD) analysis was conducted using a XPertProPW3050/60X-ray diffractometer (Cu*K*α radiation, λ = 0.15406 nm). The observed vibrational bands were investigated by FTIR spectroscopy using Thermo NicoletiS5. FESEM was analyzed to investigate the morphological characteristics using the CARL 5ZEISS-SIGMA300 equipment. Energy-dispersive X-ray (EDX) analysis and EDX elemental mapping of the samples were conducted concurrently with field emission scanning electron microscopy (FESEM) instrument. The shape and structure of nanoparticles were assessed at FEI Technai G2 20 S-TWIN transmission electron microscope (TEM) with low to high resolution. X-ray photoelectron spectroscopy (XPS) tests were conducted using an improved ALU-PHI 5000 VER instrument with Mg*K*α radiation (hν = 1256.3 eV) or Al*K*α radiation (hν = 1486.6 eV). The optical properties were studied by using the JASCO V-670 spectrophotometer. The electrochemical measurement of a Fe_3O_4:Gd @$NaYF_4$ electrode was assessed in a 6 M KOH electrolyte at room temperature using auto lab equipment.

RESULTS AND DISCUSSION

Thermal studies: The thermal property of the as-prepared sample was examined using the TG-DTA analysis and the result is illustrated in Fig. 1. The two stages of sample decomposition were observed to occur at temperatures ranging from 0 to 1000 ºC, as indicated by the TGA curve. The primary weight loss of 13% was observed at 30º to 160 ºC as a result of the loss of water molecules. The complete removal of carbon templates and organic residues was the cause of the significant mass loss of 6% between the temperatures of 161 ºC and 700 ºC. Moreover, there was no visible weight loss recorded above 700 ºC and the lack of an exothermic peak indicated the completion of the oxidation process of the precursor. The endothermic peaks observed at 200 ºC and 560 ºC corresponded to the degradation of hydroxide material and the phase transition of the product.

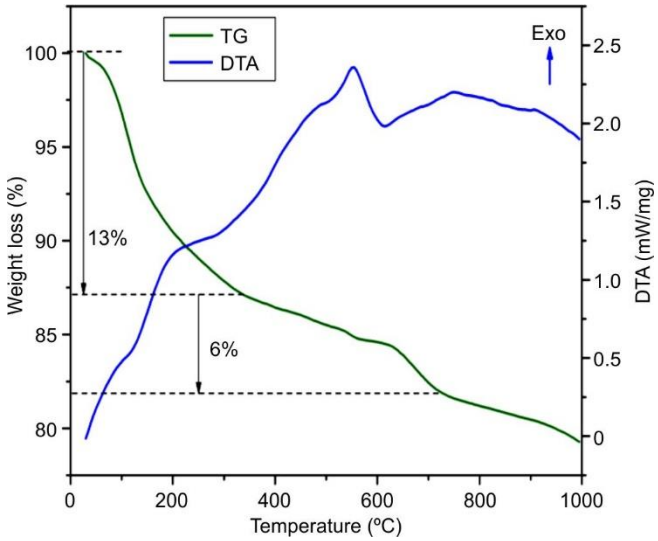

Fig. 1. TG-DTA analysis of as-prepared sample

XRD studies: The XRD pattern was employed to analyze the crystal structures of Fe_3O_4:Gd and Fe_3O_4:Gd@$NaYF_4$ core-shell nanoparticles. Fig. 2 showed that the XRD diffraction patterns of Fe_3O_4:Gd nanoparticles was observed at (220), (311), (400), (422) and (440), correspond to the peak positions of 30.72º, 35.44º, 43.05º, 53.93º and 62.34º, respectively. The obtained diffraction peaks are cubic crystal structure and good matched with standard JCPDS no. 89-3854 [21]. The XRD pattern of Fe_3O_4:Gd@$NaYF_4$ core-shell nanoparticles, where diffraction peaks associated with both Fe_3O_4:Gd and $NaYF_4$ are observable, confirming the existence of both components in the core-shell nanoparticles. The influence of $NaYF_4$in host lattice the crystallinity and crystallite size progressive sharpening of the XRD peaks. The sharp and high intensity of diffraction peaks indicated that Fe_3O_4:Gd@$NaYF_4$ core-shell nanoparticles had a good crystalline nature. The crystallite size was examined using the Debye Scherrer's formula expressed as follows [22]:

$$D = \frac{0.89\lambda}{\beta \cos\theta} \quad (1)$$

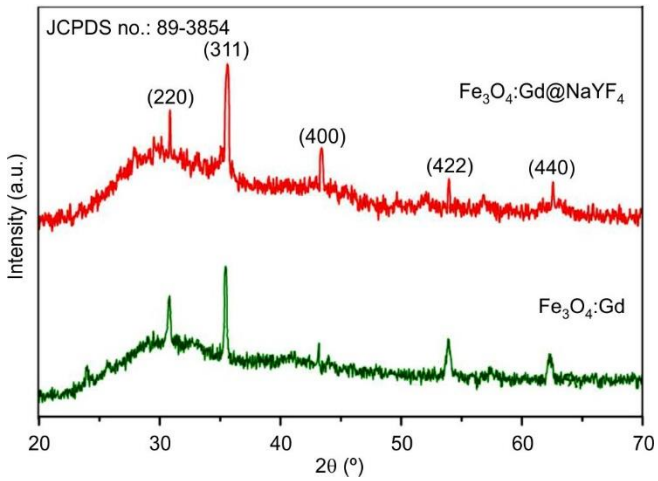

Fig. 2. XRD patterns of Fe_3O_4:Gd and Fe_3O_4:Gd@$NaYF_4$ core-shell nanoparticles

where λ = wavelength; β = the full width at half maximum; and D = the crystallite size; and θ = the Bragg's angle. The evaluated crystallite sizes were found to be 58 and 62 nm corresponding to the Gd-Fe_3O_4 and Fe_3O_4:Gd@$NaYF_4$ core-shell nanoparticles, respectively. The crystallite size increased due to the diffraction peaks become sharper. These changes suggest improved crystallite growth and improved long-range order within the crystal structure. The enhanced crystallinity typically results in better charge transport pathways and reduced internal resistance, which are essential for high-rate electrochemical performance. At the same time, moderate crystallite growth can increase the number of active sites for redox reactions without severely compromising surface area. This structural evolution correlates well with the observed enhancement in specific capacitance.

FTIR spectral studies: The characteristic inter-atomic bands formed between the constituent elements of the proposed material was analyzed *via* infrared spectra, as shown in Fig. 3. The introduction of rare earth ions in Fe_3O_4 results in various physical and structural modifications. The structural modifications induced by metal ions significantly influenced the lattice vibrations. Furthermore, various factors including cation mass, cationic oxygen and bonding force influence the lattice vibrations that vary with dopant concentration. The strong vibration bands appeared at 593, 1082, 1371, 1604 and 3454 cm^{-1} for both samples. The broad bands located at 3454 and 1604 cm^{-1} were attributed to the stretching and bending vibrations of water molecules, respectively [23,24]. The absorption bands at 1082 and 1371 cm^{-1} was consistent with the -C-O and -C=O stretching bands, respectively [25]. The bands at 593 cm^{-1} are due to the metal-oxygen bonding. Two primary

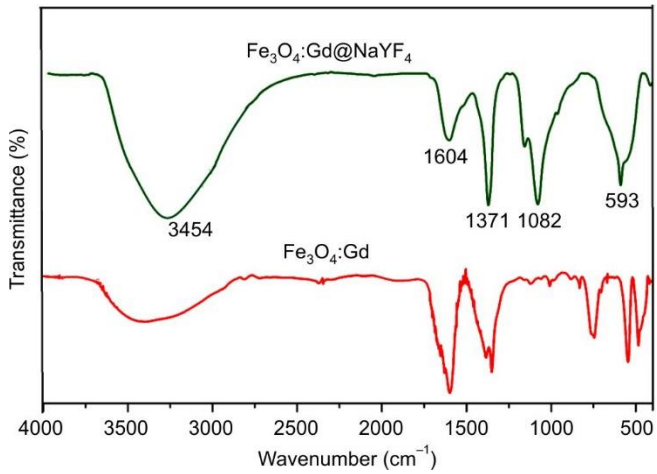

Fig. 3. FTIR spectrum of Fe_3O_4:Gd and Fe_3O_4:Gd@$NaYF_4$ core-shell nanoparticles

absorption bands emerged at approximately 443 cm^{-1} and 586 cm^{-1}, attributable to the stretching vibrations of the octahedral and tetrahedral metal-oxygen (Gd/Fe-O) ions, respectively [26].

Morphological studies: The morphology of the synthesized core-shell nanoparticles was examined using field emission scanning electron microscopy (FESEM). As shown in Fig. 4a-b, the Fe_3O_4:Gd nanoparticles are relatively monodisperse and exhibit a spherical morphology. The images of the Fe_3O_4:Gd@$NaYF_4$ core-shell nanoparticles in Fig. 4d-e reveal a significant change in particle size and morphology due to the $NaYF_4$ shell deposition. Remarkably, the resulting core-shell nanoparticles are spherical and interconnected,

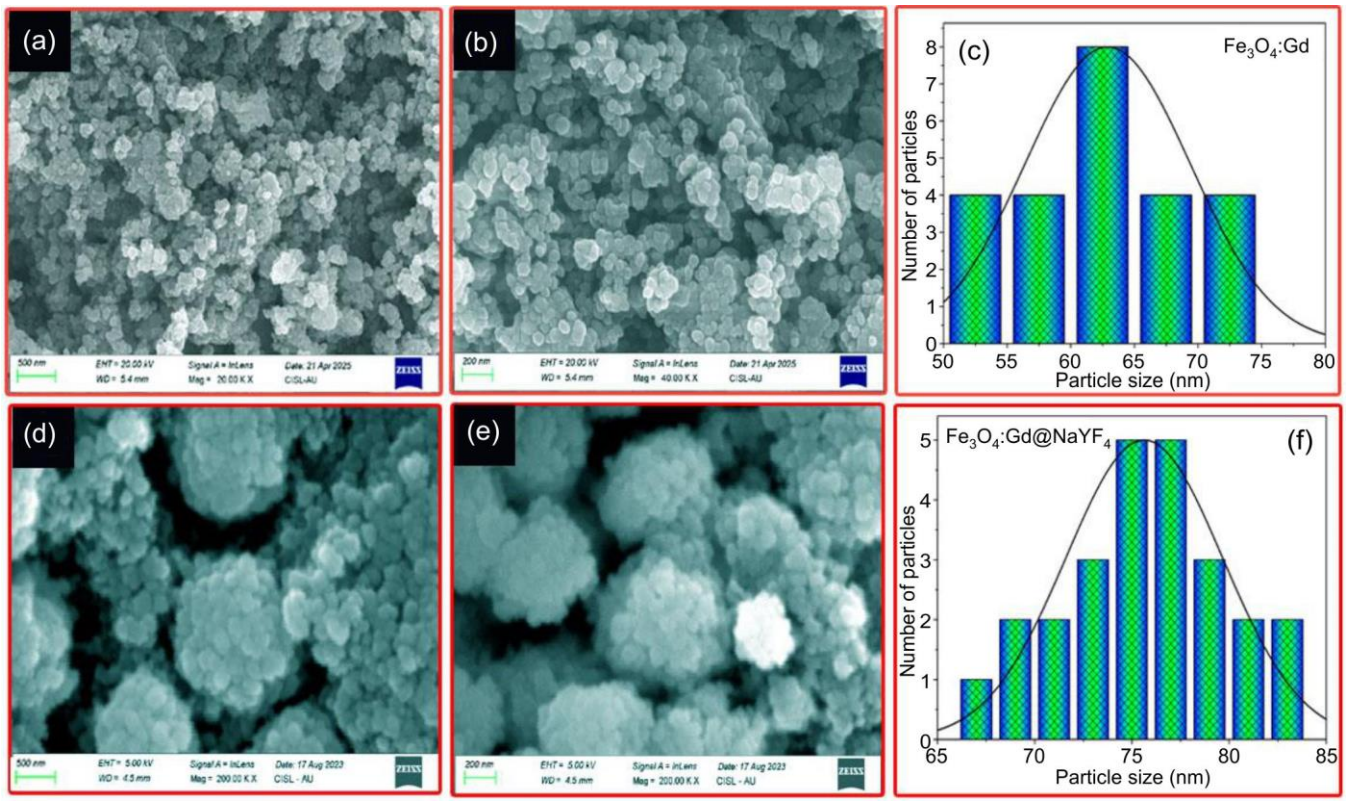

Fig. 4. FESEM images (a,b) Fe_3O_4:Gd, (d,e) Fe_3O_4:Gd@$NaYF_4$ core-shell nanoparticles and corresponding histogram images (c,f)

forming clustered structures. Also, the clustered spherical Fe_3O_4:Gd@$NaYF_4$ core-shell nanoparticles enhance specific capacitance by maximizing the electroactive surface area for ion interaction and developing an interconnected conductive network for fast charge transfer. The $NaYF_4$ shell stabilizes the redox activity of Fe_3O_4 core, improving cycle ability, while the clustered, open structure ensures efficient electrolyte penetration and accommodates structural changes during cycling. The histogram analysis reveals average grain sizes of 62 nm and 75 nm for the Fe_3O_4:Gd and Fe_3O_4:Gd@$NaYF_4$ core-shell samples, as illustrated in Fig. 4c,f.

EDS mapping studies: EDS mapping was utilized to quantify the chemical composition of both samples, as shown in Fig. 5a-f. The elemental mapping spectrum distinctly illustrates the aerial distribution of the elements detected in the prepared samples. The uniform distribution of spots in the EDS mapping indicated the presence of Fe, Gd, Na, Y, F and O elements. Moreover, the spectra demonstrated the absence of supplementary components and confirmed that the synthesized samples were Fe_3O_4:Gd@$NaYF_4$ core-shell nanoparticles.

HRTEM: HRTEM images were utilized to examine the structure and dimensions of the Fe_3O_4:Gd and Fe_3O_4:Gd@$NaYF_4$ core-shell nanoparticles. The HRTEM images exhibited the spherical particles and cluster type formation for Fe_3O_4:Gd and Fe_3O_4:Gd@$NaYF_4$ core-shell nanoparticles, respectively (Fig. 6a-b,e-f). This core-shell structure is anticipated to deliver exceptional performance in a supercapacitor, owing to the synergistic interactions between the three materials. The lattice spacing values of both samples are shown in Fig. 6c,g and measured value at 0.25 nm and 0.34 nm, corresponding to the (311) and (111) crystallographic plane of Fe_3O_4:Gd and Fe_3O_4:Gd@$NaYF_4$ core-shell nanoparticles, respectively. The HRTEM pictures revealed the SAED patterns of both samples, displaying strong diffraction spots, indicating that both samples were polycrystalline (Figs. 6d,h). The obtained results were consistent with the FESEM findings.

XPS studies: The X-ray photoelectron spectroscopy (XPS) was employed to ascertain the presence of constituent elements, their chemical states and the successful substitution of Gd@$NaYF_4$ ions into the Fe_3O_4 host material. The XPS spectra of Fe_3O_4:Gd@$NaYF_4$ core-shell nanoparticles were investigated to their electronic interactions, with the results are shown in Fig. 7. The survey scan spectrum (Fig. 7a) indicates the presence of Fe 2*p*, Gd 4*d*, Na 1*s*, Y 3*p*, F 1*s* and O 1*s*, thereby confirming the existence of $NaYF_4$ in the core-shell as demonstrated by the survey spectrum. Fig. 7b displayed the two high-resolution major characteristics peaks Fe $2p_{1/2}$ and Fe $2p_{3/2}$ located at 711.6 and 725.5 eV, respectively [27]. The distance between the two prominent peaks was approximately 14.1 eV. Furthermore, the estimated value of Fe^{2+} agreed with the observed segregation of energy levels within the structure. The binding energies of 141.8 and 147.6 eV correspond to the two largest peaks seen at Gd $4d_{5/2}$ and Gd $4d_{3/2}$ (Fig. 7c). The distance between the above two binding energies is approximately 6.1 eV [28]. From the O1s spectrum (Fig. 7d), it can be observed the band can be located at 531.5 (O_{ads}) and defined as O_{ads} is the absorbed oxygen ions in the oxygen

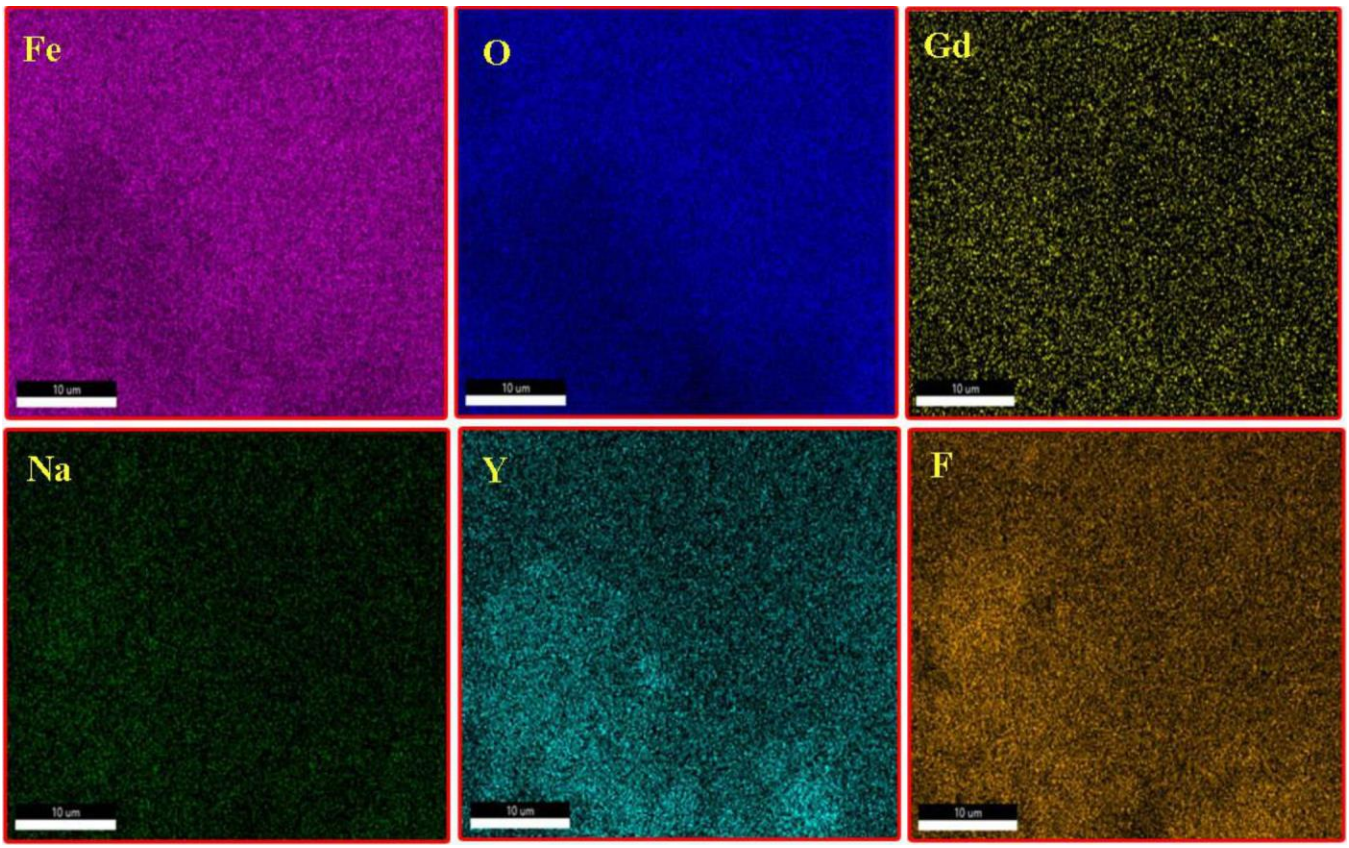

Fig. 5. EDS mapping spectrum of Fe_3O_4:Gd@$NaYF_4$ core-shell nanoparticles

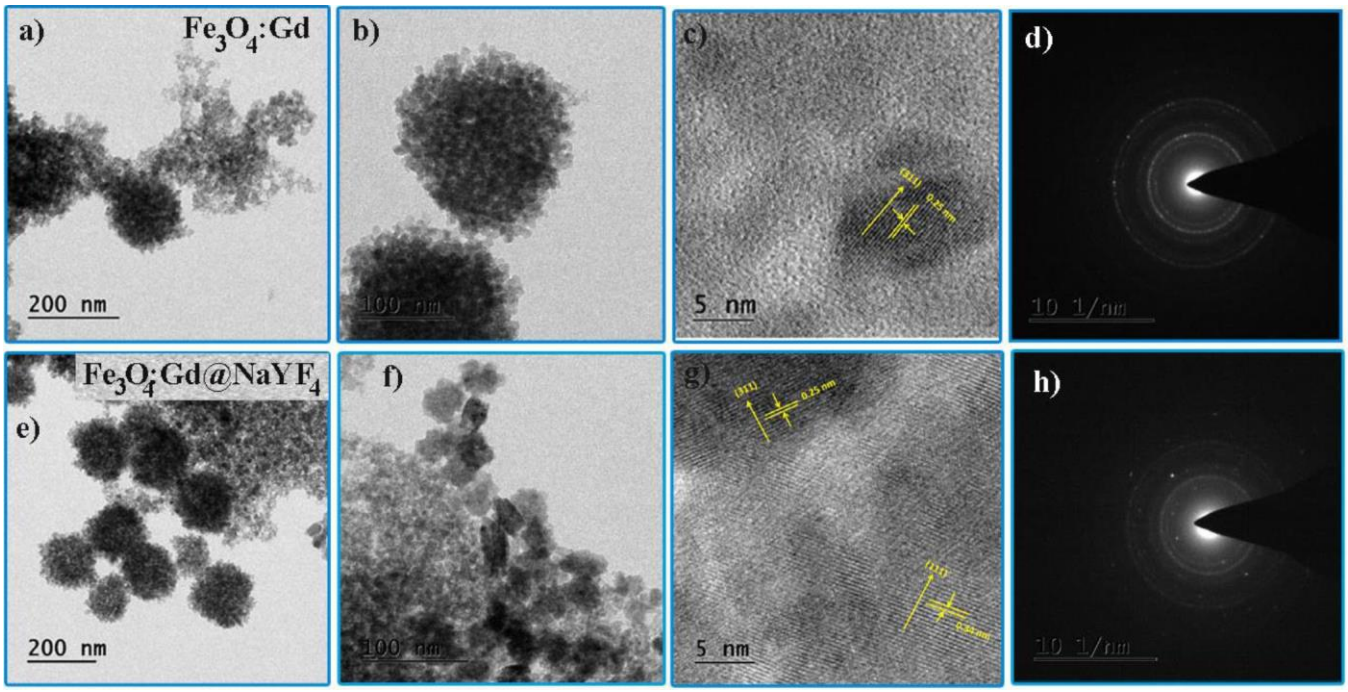

Fig. 6. HRTEM analysis of Fe_3O_4:Gd nanoparticles (a,b) images (c) lattice spacing, (d) SAED pattern and Fe_3O_4:Gd@$NaYF_4$ core-shell nanoparticles (e,f) images,(g) lattice spacing, (h) SAED pattern

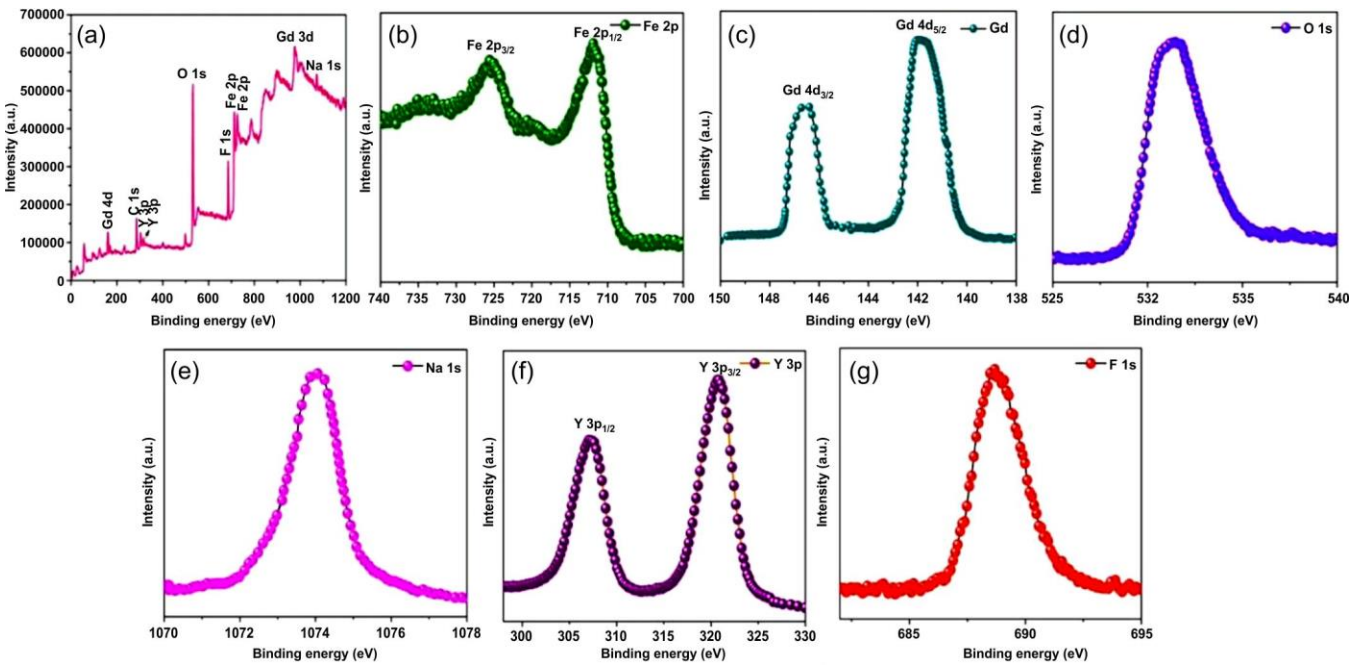

Fig. 7. XPS spectrum of Fe_3O_4:Gd@$NaYF_4$ core-shell nanoparticles (a) survey scan, (b) Fe 2P, (c) Gd 3d, (d) O 1s, (e) Na 1s, (f) Y 3p, (g) F 1s

deficient regions. This behaviour shows that there is not just lattice oxygen but also adsorption oxygen in the sample. These functional groups enhance capacitive performance by contributing to extra pseudocapacitance and improving the wettability between the electrode and electrolyte [29]. The Na 1*s* spectra are shown in Fig. 7e, where a binding energy peak is present at 1074 eV for Fe_3O_4:Gd@$NaYF_4$. The observed binding energy confirmed the Na^+ state for Fe_3O_4:Gd@$NaYF_4$ core-shell nanoparticles [30]. Fig. 7f presents the high-resolution spectra of Y 3*p*, revealing two binding energy peaks at 320.2 eV and 308.5 eV corresponding to the Y $3p_{3/2}$ and Y $3p_{1/2}$ states, respectively, indicating the Y^{3+} state. The F 1*s* XPS spectra depicted in Fig. 7g for Fe_3O_4:Gd@$NaYF_4$ core-shell nanoparticles exhibit binding energy peak at 688.4 eV, confirming the -1 oxidation state of fluorine [31].

Optical properties: UV-Vis spectroscopy measurement was performed with Fe_3O_4:Gd and Fe_3O_4:Gd@$NaYF_4$ core-shell nanoparticles to determine their optical properties and

the spectra are presented in Fig. 8a. The Fe_3O_4:Gd@$NaYF_4$ core-shell nanoparticles demonstrate improved absorption in the visible spectrum. Fig. 8 clearly revealed that the light absorption characteristics of Fe_3O_4:Gd@$NaYF_4$ core-shell nanoparticles are augmented across the whole visible spectrum. This alteration in the electronic configuration of core-shell structures may enhance electrochemical performance, resulting in increased fast ion transport in $NaYF_4$ and expedited the transport to reaction sites.

The energy band gap can be difficult to estimate directly from absorption spectra; consequently, it is determined by Tauc's plots using eqn. 2 [32].

$$\alpha h\nu = A(h\nu - E_g)^n \quad (2)$$

where h is excitation energy; E_g is the optical band gap, α is the proportionality parameter that depends on electron transition probability; and n is the index number that signifies the nature of the energy band transition. The direct permitted transition is quantified by selecting the appropriate exponent value, specifically n = 1/2. Fig. 8b represents the optical bandgap of Fe_3O_4:Gd and Fe_3O_4:Gd@$NaYF_4$ core-shell nanoparticles and plots the linear part of $(\alpha h\nu)^2$ *versus* hν. The calculated bandgap values were 3.60 eV and 3.25 eV for Fe_3O_4:Gd and Fe_3O_4:Gd@$NaYF_4$ core-shell nanoparticles, respectively. The decrease in bandgap values with increasing crystallite size can be attributed quantum confinement effect, wherein finite numbers of an atom are tightly bonded with each other than a bigger crystallite size. Consequently, the overlap between atomic orbitals intensifies with an increase in crystallite size. The overlap of orbitals introduces intermediate energy levels within the band gap leading to band gap narrowing. Therefore, this alteration in band gap may occur as the crystallite size enlarges with the augmentation of $NaYF_4$ concentration [33].

Magnetic analysis: The magnetic characteristics of prepared core-shell nanoparticles were investigated using a vibrating sample magnetometer (VSM) at room temperature. It was found that both samples have strong magnetic responses to a changing magnetic field. The shift in magnetization (M) in emu g^{-1} as a function of an applied magnetic field (H) in the range of -15000 Oe to 15000 Oe is shown in Fig. 9. According to the hysteresis loop, every single nanoparticle exhibited super ferromagnetic properties. The saturation magnetization (M_s) value of Fe_3O_4:Gd and Fe_3O_4:Gd@$NaYF_4$ core-shell nanoparticles is 51.08 emu g^{-1} and 32.65 emu g^{-1}, respectively. The presence of a nonmagnetic $NaYF_4$ shell on the surface of Fe_3O_4 core nanoparticles causes a reduction in saturation magnetization. In addition, the magnetic moment of the magnetite core decreases at the core-shell interface as a result of magnetite interaction with the $NaYF_4$ shell and the shielding effect of the $NaYF_4$ shell. The shielding effect of a $NaYF_4$ shell is determined by the ratio of the diamagnetic coating mass volume to the entire sample volume and hence the shell's thickness. The coercivity (M_r) (strength of reverse field required to return material to zero magnetization state) values of Fe_3O_4:Gd 3.68 Oe reduces to 2.25 Oe for Fe_3O_4:Gd @$NaYF_4$ core-shell nanoparticles, respectively. This reduction could be attributable to decreased interparticle interactions and magnetoelastic anisotropy. As the $NaYF_4$ shell surrounds the magnetic core of Gd:Fe_3O_4, the surface stress of the magnetic nanoparticles increases, resulting in an increase in magnetoelastic anisotropy. The core-shell sample exhibit low coercivity, resulting in superparamagnetic $NaYF_4$ coated Fe_3O_4 nanoparticles. The remanence (H_c) values (value of magnetization at zero field) of 5.16 Oe and 3.69 emu/g for Fe_3O_4:Gd and Fe_3O_4:Gd@$NaYF_4$ core-shell nanoparticles, respectively. According to this study, the magnetic performance of Fe_3O_4:Gd has improved *via* the incorporation of $NaYF_4$ cations into the magnetite crystal structure. Furthermore, these magnetic values suggest the suitability of the prepared superparamagnetic Fe_3O_4:Gd@$NaYF_4$ core-shell nanoparticles for biomedical and supercapacitor applications.

Electrochemical analysis

Cyclic voltammetry: In order to assess the potential applications in electrochemical capacitors, the Fe_3O_4:Gd and

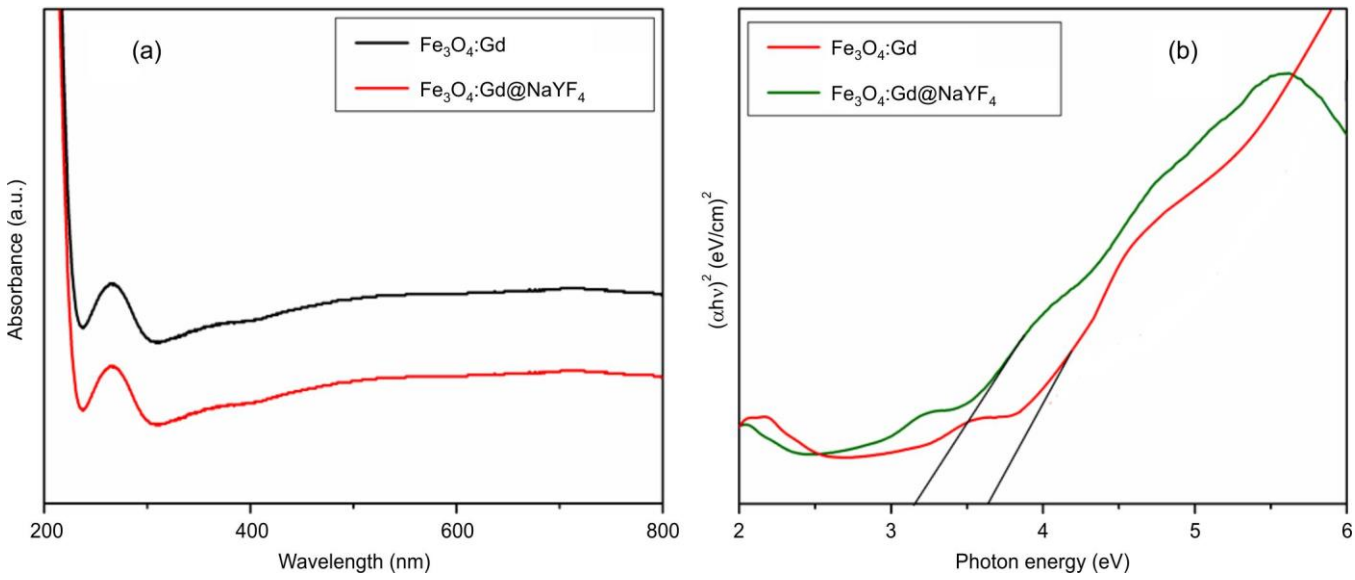

Fig. 8. Optical properties of Fe_3O_4:Gd and Fe_3O_4:Gd@$NaYF_4$ core-shell nanoparticles (a) UV-Vis, (b) bandgap

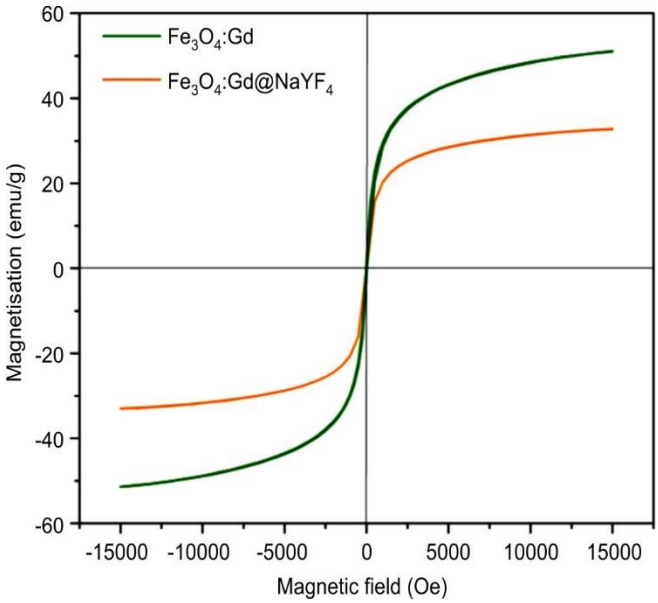

Fig. 9. VSM analysis of Fe_3O_4:Gd and Fe_3O_4:Gd@$NaYF_4$ core-shell nanoparticles

Fe_3O_4:Gd@$NaYF_4$ core-shell nanoparticles was employed to fabricate electrodes in a three-electrode configuration. The CV profile of the Fe_3O_4:Gd@$NaYF_4$ electrode in 6 M KOH aqueous electrolyte at varying scan rates are shown in Fig. 10. The CV curves shape deviates from the ideal rectangle, indicating the Faradic pseudocapacitive character of the electrode, despite the absence of distinct redox peaks. Moreover, with an increase in the scan rate, primarily rectangular shapes accompanied by oxidation/reduction peaks persist, suggesting that the electrode demonstrates significant reversibility and stability within the previously established optimal range. The specific capacitance was assessed using cyclic voltammetry using the following formula [34]:

$$C_s = \frac{\int Idv}{m \times s \times V} \quad (3)$$

where I·dv is the charge obtained from the CV curves; m is the mass of active material in the electrode (mg); V is the potential window; and s is the scan rate (mV/s). According to the CV curves, Fe_3O_4:Gd electrode exhibited the capacitance values of 520, 485, 432, 393, 330, 272 and 230 F g^{-1} at scan rates of 5, 10, 15, 25, 50, 75 and 100 mV s^{-1}, respectively. Likewise, the Fe_3O_4:Gd@$NaYF_4$ electrode had maximum capacitance values of 565, 531, 460, 366, 264, 248 and 216 F g^{-1} at 5, 10, 15, 25, 50, 75 and 100 mV s^{-1}, respectively. The integration of $NaYF_4$ with Gd-doped Fe_3O_4 nanoparticles enhances electrochemical performance through synergistic improvements in stability and charge transfer. The robust, inert $NaYF_4$ shell prevents the oxidation, dissolution and agglomeration of the Fe_3O_4 core, ensuring long-term structural integrity. Furthermore, the Fe_3O_4:Gd interface can mediate ion conduction and reduce charge recombination, while the $NaYF_4$ interface can mediate ion conduction and reduce charge recombination, while lanthanide ions introduce active sites that improve reactant adsorption [35,36].

Galvanostatic charge discharge analysis: The galvanostatic charge discharge curves of the Fe_3O_4:Gd and Fe_3O_4:Gd@$NaYF_4$ core-shell nanoparticles electrodes, which were prepared at varying current densities, are exhibited in Fig. 11. The potential range is 0-0.25 V, which further confirms the pseudocapacitance behaviour of the both prepared electrodes, as the peaks observed in the CV curves are well-matched by the nonlinear discharge curves and the voltage plateaus. The specific capacitance was calculated using charge-discharge curves using the following formula [37]:

$$C_s = \frac{i\Delta t}{m\Delta v} \quad (4)$$

where i denoted the discharge current; m denoted the mass of active material; Δt denoted the discharge time; and ΔV denoted the potential change during the discharge. The measured capacitance (C_{sp}) values of the Fe_3O_4:Gd electrode showed 580, 460, 324, 288, 231 F g^{-1} for various current densities of 1, 2, 3, 4 and 5 A g^{-1}, respectively. Subsequently, the Fe_3O_4:Gd@$NaYF_4$ electrode exhibited specific capacitance values of 612,

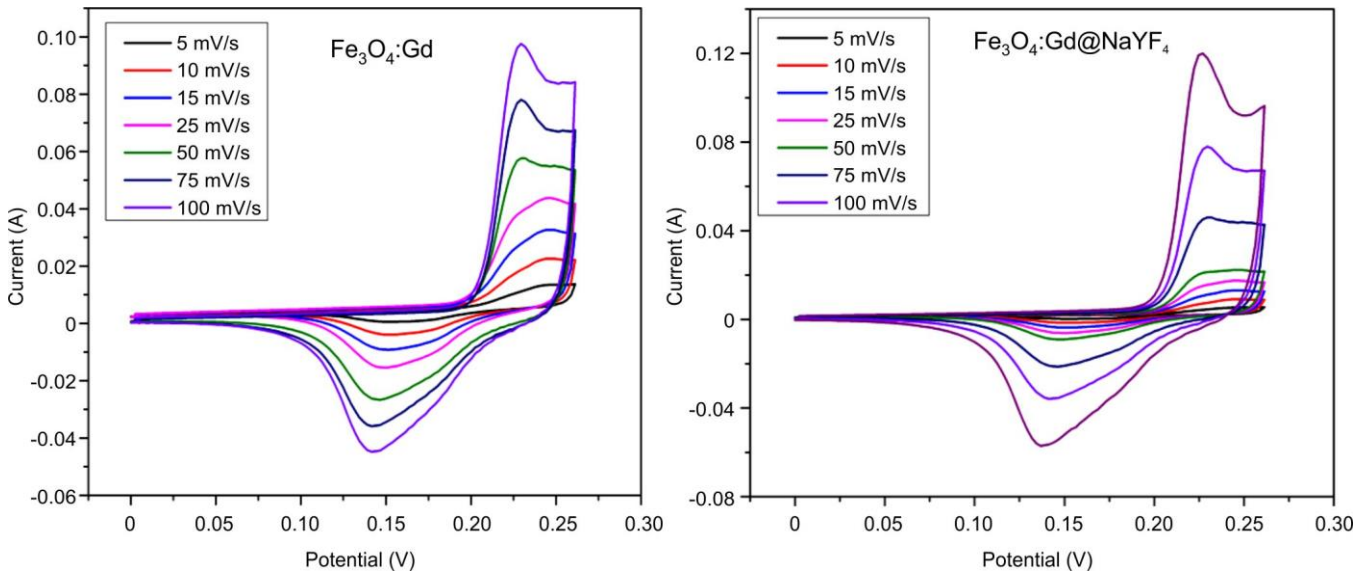

Fig. 10. Cyclic voltammetry spectrum of Fe_3O_4:Gd and Fe_3O_4:Gd@$NaYF_4$ core-shell nanoparticles

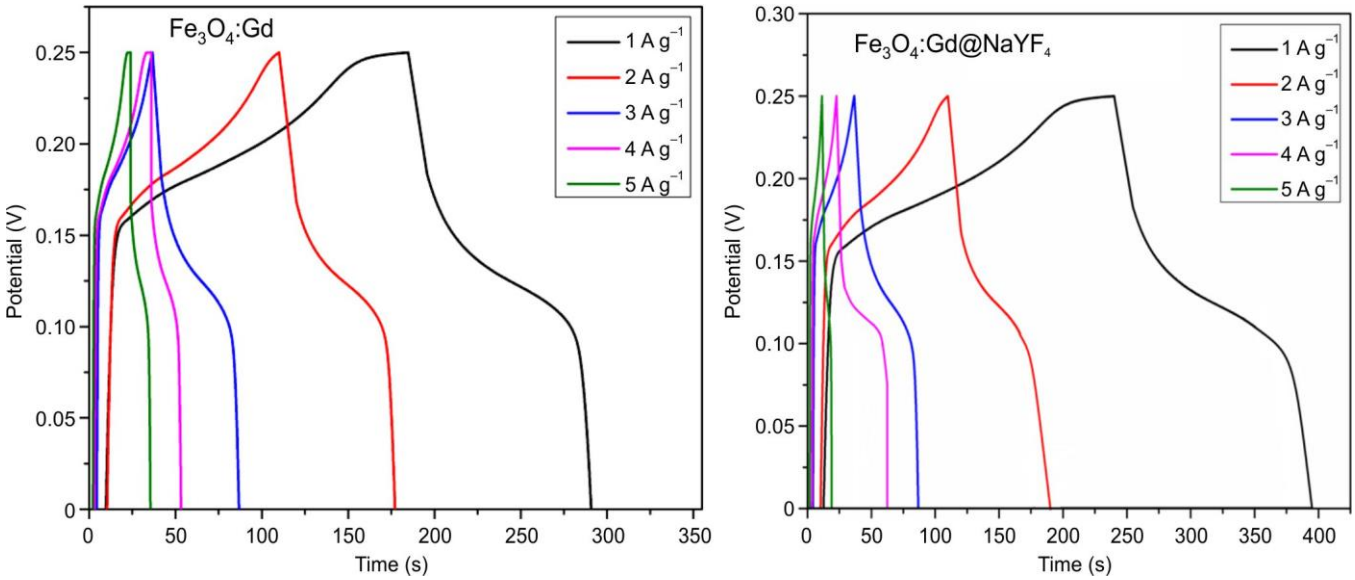

Fig. 11. Galvanostatic charge and discharge profile of Fe_3O_4:Gd and Fe_3O_4:Gd@$NaYF_4$ core-shell nanoparticles

TABLE-2
COMPARISON OF THE CAPACITANCE OF Fe_3O_4:Gd@$NaYF_4$ CORE-SHELL NANOPARTICLES WITH OTHER REPORTED CORE-SHELL NANOPARTICLES

Core-shell structure	Method	Capacitance value	Test conditions	Ref.
Fe_3O_4@C@MnO_2	Stöber method	158 F g^{-1}	0.5 A g^{-1}	[38]
α-Fe_2O_3@CeO_2	Simple method	168 F g^{-1}	5 mV s^{-1}	[39]
Fe_3O_4 (G/Co/F-NCs)	Co-precipitation method	184 F g^{-1}	1 A g^{-1}	[40]
Fe_3O_4@C@PANI	Hydrothermal method	322.5 F g^{-1}	2.5 A g^{-1}	[41]
Fe_3O_4@CAs	Hydrothermal method	342.1 F g^{-1}	0.5 A g^{-1}	[42]
Fe_3O_4:Ce@$NaYF_4$	Hydrothermal method	528 F g^{-1}	1 A g^{-1}	[43]
Fe_3O_4:Gd@$NaYF_4$	Hydrothermal method	612 F g^{-1}	1 A g^{-1}	Present work

563, 485, 352 and 240 F g^{-1} for different current densities of 1, 2, 3, 4 and 5 A g^{-1}, respectively. The GCD results demonstrate that the Fe_3O_4:Gd@$NaYF_4$ electrode presents a higher specific capacitance in comparison to the Fe_3O_4:Gd electrode, attributable to the enhancement in specific capacitance values facilitated by the presence of $NaYF_4$ ions. In comparison to Fe_3O_4:Gd electrodes, the Fe_3O_4:Gd@$NaYF_4$ core-shell nanoparticles exhibited elevated current densities and an increased surface area, indicating a substantial improvement in capacitance attributed to various electron transport pathways and the synergistic interactions among the $NaYF_4$ and Fe_3O_4:Gd. Table-2 shows the comparison of the capacitance of Fe_3O_4:Gd @$NaYF_4$ core-shell nanoparticles with other reported core-shell nanoparticles.

Electrochemical impedance spectroscopy (EIS): To examine the charge carrier transport characteristics, electrochemical impedance spectroscopy (EIS) was performed on Fe_3O_4:Gd and Fe_3O_4:Gd@$NaYF_4$ electrodes. The Nyquist plots for both electrodes display a semicircle in the high-frequency region and an inclined line in the low-frequency region. Fig. 12 shows that the Fe_3O_4:Gd@$NaYF_4$ electrode has a smaller high-frequency intercept and a steeper low-frequency slope compared to Fe_3O_4:Gd. This indicates lower internal resistance, improved charge transfer and faster ion diffusion in the core-shell structure. The enhanced performance is attributed to the spherical morphology and higher electrical conductivity

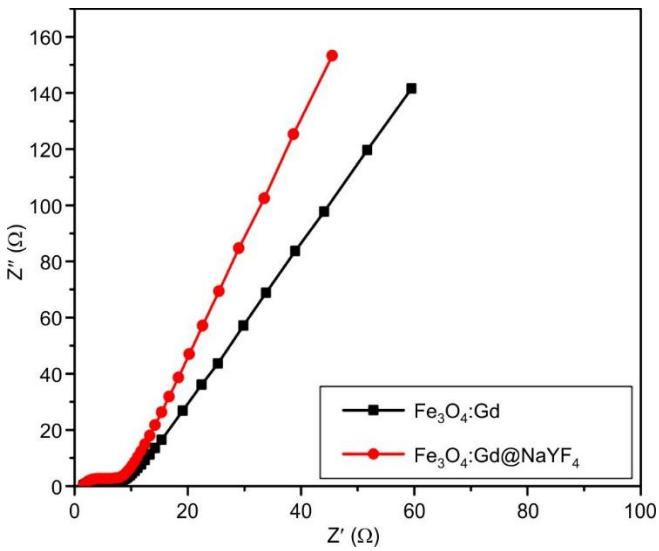

Fig. 12. EIS spectrum of Fe_3O_4:Gd and Fe_3O_4:Gd@$NaYF_4$ core-shell nanoparticles

of the $NaYF_4$ shell, which increases specific surface area and facilitates ion transport, thereby improving capacitance [44].

Conclusion

Fe_3O_4:Gd@$NaYF_4$ core-shell nanoparticles were synthesized *via* a hydrothermal method. The XRD results confirmed

the cubic Fe_3O_4:Gd core and $NaYF_4$ shell without structural modification. FTIR confirmed metal oxide bands and XPS verified Na^+ and Y^{3+} oxidation states. The FESEM and HRTEM studies revealed the Fe_3O_4:Gd@$NaYF_4$ core-shell nanoparticles exhibited spherical like structures. The magnetic, Gd doped Fe_3O_4 core improves electron mobility and conductivity, while the $NaYF_4$ shell enhances stability and prevents agglomeration. This synergistic core-shell structure enables high specific capacitance (612 F g^{-1}) and improved charge-discharge efficiency. Furthermore, the incorporation of rare-earth elements like Gd introduces tuneable properties, which can be tailored for multifunctional energy storage systems.

CONFLICT OF INTEREST

The authors declare that there is no conflict of interests regarding the publication of this article.

DECLARATION OF AI-ASSISTED TECHNOLOGIES

During the preparation of this manuscript, the authors used an AI-assisted tool(s) to improve the language. The authors reviewed and edited the content and take full responsibility for the published work.

REFERENCES

1. Y. Wang, L. Zhang, H. Hou, W. Xu, G. Duan, S. He, K. Liu and S. Jiang, *J. Mater. Sci.*, **56**, 173 (2021); https://doi.org/10.1007/s10853-020-05157-6
2. F. Ahmad, M. Zahid, H. Jamil, M.A. Khan, S. Atiq, M. Bibi, K. Shahbaz, M. Adnan, M. Danish, F. Rasheed, H. Tahseen, M.J. Shabbir, M. Bilal and A. Samreen, *J. Energy Storage*, **72**, 108731 (2023); https://doi.org/10.1016/j.est.2023.108731
3. M. Yang, K. Chen, H. Li, Y. Cao, H. Yang and X. Ai, *Adv. Funct. Mater.*, **33**, 2306828 (2023); https://doi.org/10.1002/adfm.202306828
4. F. Ali and N.R. Khalid, *Ceram. Int.*, **46**, 24137 (2020); https://doi.org/10.1016/j.ceramint.2020.06.193
5. I. Poimenidis, E. Skliri, V. Binas, K. Komnitsas and M. Konsolakis, *Next Mater.*, **10**, 101449 (2026); https://doi.org/10.1016/j.nxmate.2025.101449
6. M.J. Pang, G.H. Long, S. Jiang, Y. Ji, W. Han, B. Wang, X.L. Liu, Y.L. Xi, D.X. Wang and F.Z. Xu, *Chem. Eng. J.*, **280**, 377 (2015); https://doi.org/10.1016/j.cej.2015.06.053
7. M.J. Salethraj, G.D. Jeyaleela, D. Govindarajan, L. Guganathan, M. Abbas, S. Kalathil and A. Raja, *J. Mater. Sci. Mater. Electron.*, **37**, 119 (2026); https://doi.org/10.1007/s10854-025-16507-y
8. D. Ahamada, P. Baraneedharan, P. Ramakrishnan and S.B. Mohamed, *J. Mater. Sci. Mater. Electron.*, **37**, 100 (2026); https://doi.org/10.1007/s10854-025-16447-7
9. M. Talha and S. Karamat, in eds.: M. Jawaid, R. Khiari and B. Singh, Structural Characterization of Nanocellulose and Fe_3O_4 Hybrid Nanomaterials, In: Properties and Characterization of Nanocellulose and Nanocellulose-Based Composites, Woodhead Publishing, Chap. 16, pp. 525-545 (2026).
10. Nasrullah, W. Wisal, F. Bibi, S.K. Shah, J. Ullah, M. Rauf, R. Gunnella, S.S. Shah, T. Ogawa, M.A. Aziz and K. Hayat, *J. Inorg. Organomet. Polym.*, (2026); https://doi.org/10.1007/s10904-025-04169-6
11. G. Srivastava, Ravina, S. Dalela, N.K. Gautam, S. Kumar, S.Z. Hashmi, M.A. Ahmad, A.M. Quraishi, V. Khanna and P.A. Alvi, *Nano Trends*, **9**, 100067 (2025); https://doi.org/10.1016/j.nwnano.2024.100067
12. A.U. Rehman, M. Atif, M. Younas, T. Rafique, H. Wahab, A. UlHamid, N. Iqbal, Z. Ali and W. Khalid, *RSC Adv.*, **12**, 12344 (2022); https://doi.org/10.1039/D2RA00530A
13. P. Akhtar, M.N. Akhtar, M.A. Baqir, A. Ahmad, M.U. Khallidoon, M. Farhan and M.A. Khan, *J. Mater. Sci. Mater. Electron.*, **32**, 7692 (2021); https://doi.org/10.1007/s10854-021-05487-4
14. J. Majeed, J. Ramkumar, S. Chandramouleeswaran and A.K. Tyagi, *AIP Conf. Proc.*, **1591**, 605 (2014); https://doi.org/10.1063/1.4872690
15. D. Shi, H. Yang, S. Ji, S. Jiang, X. Liu and D. Zhang, *Procedia Eng.*, **102**, 1555 (2015); https://doi.org/10.1016/j.proeng.2015.01.291
16. K.P. Hazarika, R. Fopase, L.M. Pandey and J.P. Borah, *Physica B: Conden. Matter.*, **645**, 414237 (2022); https://doi.org/10.1016/j.physb.2022.414237
17. S. Khashan, S. Dagher, N. Tit, A. Alazzam and I. Obaidat, *Surf. Coat. Technol.*, **322**, 92 (2017); https://doi.org/10.1016/j.surfcoat.2017.05.045
18. C. Homann, L. Krukewitt, F. Frenzel, B. Grauel, C. Würth, U. Resch-Genger, and M. Haase, *Angew. Chem.*, **57**, 8765 (2018); https://doi.org/10.1002/anie.201803083
19. X. Cui, D. Mathe, N. Kovács, I. Horváth and M. Jauregui-Osoro, *Bioconjugate Chem.*, **27**, 319 (2016); https://doi.org/10.1021/acs.bioconjchem.5b00338
20. J.C. Boyer, L.A. Cuccia and J.A. Capobianco, *Nano Lett.*, **7**, 847 (2007); https://doi.org/10.1021/nl070235+
21. L. Chen, Q. Zhou, Q. Xiong, W. Li, J. Liu and X. Yang, *Adv. Mater. Sci. Eng.*, **2015**, 763124 (2015); https://doi.org/10.1155/2015/763124
22. I.W. Sutapa, A.W. Wahab, P. Taba and N. L. Nafie, *J. Phys.: Conf. Ser.*, **979**, 012021 (2018); https://doi.org.10.1088/1742-6596/979/1/012021
23. S. Xing, J. Zhang, Y. Li and X. Wang, *Appl. Catal. B*, **107**, 386 (2011); https://doi.org/10.1016/j.apcatb.2011.08.002
24. S. Kumari, E. Sharma, J. Verma, J. Dalal and A. Kumar, *Ceram. Int.*, **49**, 20185 (2023); https://doi.org/10.1016/j.ceramint.2023.03.142
25. J.P. Singh, G. Dixit, R.C. Srivastava, H.M. Agrawal and K. Asokan, *J. Phys. D Appl. Phys.*, **44**, 435306 (2011); https://doi.org/10.1088/0022-3727/44/43/435306
26. N. Kadian, A. Kumar, R. Singh and P. Verma, *J. Alloys Compd.*, **960**, 170811 (2023); https://doi.org/10.1016/j.jallcom.2023.170811
27. H.G. Cha, M.J. Kang, I.C. Hwang, H. Kim, K.B. Yoon, Y.S. Kang, *Chem. Commun.*, **51**, 6407 (2015); https://doi.org/10.1039/C5CC00200A
28. A.M. Faramawy, H. Elsayed, H.M. Elsayed, A.A. Sattar, Y.W. Getahun, A.A. El-Gendy and H. Kahil, *J. Alloys Compd.*, **974**, 172845 (2024); https://doi.org/10.1016/j.jallcom.2023.172845
29. Z. Li, H. Wu, D. Zhang, Q. Wang, H. Sun, Q. Sun and B. Wang, *Appl. Surf. Sci.*, **657**, 159744 (2024); https://doi.org/10.1016/j.apsusc.2024.159744
30. L. Silipigni, T. Quattrone, L. Schirò, V. Grasso, L.M. Scolaro, G. De Luca and G. Salvato, *J. Appl. Phys.*, **104**, 123711 (2007); https://doi.org/10.1063/1.3048546
31. J. Pichaandi, G.K. Das, N.J.J. Johnson, T. Regier and F.C.J.M. van Veggel, *J. Phys. Chem. C*, **118**, 21639 (2014); https://doi.org/10.1021/jp505646j
32. S. Sharma, P. Chauhan and S. Husain, *Adv. Mater. Proceed.*, **1**, 220 (2016); https://doi.org/10.5185/amp.2016/220
33. B. Shanmugapriya, N. Moorthy, P. Dhamodharan, S. Suthakaran, T. Meganathan, A. Dinesh, L. Gnanasekaran and M. Ayyar, *Inorg. Chem. Commun.*, **173**, 113763 (2025); https://doi.org/10.1016/j.inoche.2024.113763
34. S. Sivakumar and L.N. Prabu, *Inorg. Chem. Commun.*, **147**, 110247 (2023); https://doi.org/10.1016/j.inoche.2022.110247
35. M. Aghazadeh, I. Karimzadeh, M.G. Maragheh and M.R. Ganjali, *Korean J. Chem. Eng.*, **35**, 1341 (2018); https://doi.org/10.1007/s11814-018-0027-7
36. M. Mao, Q. Chen, H. Zhang, Y. Hou and J. Guo, *J. Energy Storage*, **68**, 107702 (2023); https://doi.org/10.1016/j.est.2023.107702
37. K. Manikandan, S. Dhanuskodi, N. Maheswari, G. Muralidharan, A.R. Thomas and D. Sastikumar, *RSC Adv.*, **6**, 90559 (2016); https://doi.org/10.1039/C6RA20503H

38. Z. Li, Y. Yao, Y. Zheng, T. Gao, Z. Liu and G. Zhou, *J. Electrochem. Soc.*, **165**, E58 (2018); https://doi.org/10.1149/2.0961802jes
39. M. Mazloum-Ardakani, F. Sabaghian, M. Yavari, A. Ebady and N. Sahraie, *J. Alloys Compd.*, **819**, 152949 (2020); https://doi.org/10.1016/j.jallcom.2019.152949
40. P.M. Anjana, J.F. Joe Sherin, C. Vijayakumar, S.R. Sarath Kumar, M.R. Bindhu and R.B. Rakhi, *Mater. Sci. Eng. B*, **290**, 116313 (2023); https://doi.org/10.1016/j.mseb.2023.116313
41. Q. Wu, M. Chen, K. Chen, S. Wang, C. Wang and G. Diao, *J. Mater. Sci.*, **51**, 1572 (2016); https://doi.org/10.1007/s10853-015-9480-4
42. X. Zhang, X. Wu, X. Wang, Y. Liu, B. Zhou, Y. Wang, Q. Zhu and J. Shen, *J. Energy Storage*, **72**, 108798 (2023); https://doi.org/10.1016/j.est.2023.108798
43. V. Ponni and C. Rakkappan, *Asian J. Chem.*, **37**, 2322 (2025); https://doi.org/10.14233/ajchem.2025.34339
44. Z. Elseddig, D. Wang, H. Xu and W. Zhang, *J. Alloys Compd.*, **740**, 36 (2018); https://doi.org/10.1016/j.jallcom.2017.12.368